Available online at www.sciencedirect.com

SciVerse ScienceDirect

Ceramics International 38 (2012) 6643–6649

CERAMICS INTERNATIONAL

www.elsevier.com/locate/ceramint

Structural, magnetic and photocatalytic properties of Sr^{2+}-doped $BiFeO_3$ nanoparticles based on an ultrasonic irradiation assisted self-combustion method

Ben Wang[a], Shumei Wang[a,b,*], Lixiu Gong[a], Zhufa Zhou[a,b,*]

[a]College of Chemistry, Chemical Engineering and Materials Science, Soochow University, Suzhou 215123, PR China
[b]National Engineering Laboratory of Modern Silk, Soochow University, Suzhou 215123, PR China

Received 19 March 2012; received in revised form 16 May 2012; accepted 17 May 2012
Available online 23 May 2012

Abstract

A novel ultrasonic irradiation assisted self-combustion method was developed to prepare single-phase $Bi_{1-x}Sr_xFeO_{3-\delta}$ (BSFO) nanoparticles, which were charactered by XRD, SEM, TEM and UV–vis spectra. The results show that structure, as well as magnetic and photocatalytic properties of BSFO are influenced by the particle size and the Sr^{2+} dopant content. Regarding smaller particles, even if small amount of Sr^{2+} substitution content change can result in the phase transition from the rhombohedral distorted perovskite to the cubic. The doping of heterovalent Sr^{2+} ions in $BiFeO_3$ (BFO) nanoparticles improves the ferromagnetic property. As ultrasonication can generate particles with larger surface area and more defections, BSFO nanoparticles exhibit efficient photocatalytic activity as a promising photocatalyst.

Keywords: Powders chemical preparation; Grain size; Magnetic properties; Optical properties

1. Introduction

Multiferroic materials [1,2] with significant magnetoelectric coupling have a promising prospect for the design and synthesis of multifunctional materials. Among all multiferroic materials studied so far, BFO, owning the structure of perovskite-type, has attracted more and more attention recently. BFO, with high ferroelectric Curie point ($T_c \sim 1103$ K) and G-type antiferromagnetic Néel point ($T_N \sim 647$ K), exhibits ferroelectricity and antiferromagnetic order simultaneously at room temperature. In addition to the potential magnetoelectric applications, BFO might be used in other functional fields such as visible-light photocatalytic [3], photovoltaic [4], and electromechanical [5] materials. Except for the advantages, BFO also has some defects such as the difficulty of purification, high leakage current, weak magnetic characteristics and lower magnetoelectric coupling coefficients.

Nanotechnology and metal ions doping was expected to overcome these obstacles, and the magnetic and optical properties of BFO can be improved as well. Several researchers had reported on the change of BFO properties by doping heterovalent Sr^{2+} [6–10]. Among these studies, bulk BSFO exhibits a pseudo-tetragonal crystalline structure and weak ferromagnetic at room temperature when up to 20% Sr^{2+} doping.

Though metal-ion doped BFO shows very promising properties for practical applications, the inherent antiferromagnetic ordering in bulk BFO could not provide a net magnetization [11,12]. Recently, the enhanced magnetization of nanoparticles has been reported by other reporters [13,14]. The enhancement effect is regarded as the contribution of surface-induced magnetization and oxygen deficiency. Furthermore, Selbach et al. illustrated that the phase transition from cubic structure to rhombohedral distortion is reduced by decreasing particle size [15]. Recently, a lot of specific synthesis techniques have been

*Corresponding authors. Tel.: +86 512 65880963; fax: +86 512 65880089.
E-mail address: zhouzhufa@suda.edu.cn (Z. Zhou).

0272-8842/$36.00
http://dx.doi.org/10.1016/j.ceramint.2012.05.051

employed to synthesize BFO nanoparticles, such as soft chemistry route [16], coprecipitation method [17], hydrothermal method [18] and so on. Among these methods, citrate–nitrate auto-combustion synthesis is very suitable for doping in atomic scale and low temperature synthesis, where the fuel is citric acid and metal nitrates are used as metal and oxidant sources [19]. The ultrasonic technology has also been used extensively in the preparation of materials for its cavitation phenomenon, which can generate particles with large surface area and small size [20].

In spite of the intense study, most of publications are focus on modifying the properties of BFO by doping at the Bi site in bulk BFO. However, little effort has been made towards Bi substitution by heterovalent Sr^{2+} in BFO nanoparticles [21,22]. In order to synthesize smaller particles, an ultrasonic irradiation assisted self-combustion method is reported here. The effect of the Sr^{2+} dopant concentration on the structure transformation, the ferromagnetic and the optical properties is systematically analyzed in the present paper.

2. Experimental procedures

In the synthesis procedure, samples with the nominal chemical compositions $Bi_{1-x}Sr_xFeO_{3-\delta}$ ($0 \le x \le 0.2$) were synthesized. Stoichiometric amounts of $Bi(NO_3)_3 \cdot 5H_2O$, $Fe(NO_3)_3 \cdot 9H_2O$ and $Sr(NO_3)_3 \cdot 9H_2O$ were analytical grade and used without further purification. As $Bi(NO_3)_3 \cdot 5H_2O$ undergoes precipitate of bismuth oxyhydrate in water, 15 wt% nitric acid solution was introduced in the system, and a clear and transparent final solution was obtained, suggesting the complete dissolution of $Bi(NO_3)_3 \cdot 5H_2O$. The stoichiometric amount (2:1 to metal ions in ethylene glycol) of citric acid necessary for the complete combustion of the nitrates was added, then an appropriate amount of $Fe(NO_3)_3 \cdot 9H_2O$ and $Sr(NO_3)_3 \cdot 9H_2O$ was added. The ammonia was used to tune the pH to 6 after completely mixing. The solution should be kept stirring initially at 90 °C for 2 h and continuously at 130 °C for 8 h, then the obtained sol was placed under ultrasonication with 40 kHz/200 W for 1 h at 80 °C. A self-combustion reaction took place at 250 °C, then the whole process completed within 50 s resulting in a fluffy and foamy brown mass. This porous mass was annealed at 500 °C for 2 h after grinding completely, subsequently quenched at room temperature. The obtained nanoparticles were added in 68 wt% HNO_3 with continuous stirring for 2 h. The solution was then centrifuged and dried at 80 °C to obtain the sample.

X-ray diffraction (XRD, Rigaku Dmax RB X-ray diffractometer with Cu-Ka radiation) was used for the phase identification. Scanning electron microscope (SEM, JEOL-6700F) and transmission electron microscope (TEM, TecnaiG220) were used for imagining the morphology and determining size of the sample. Magnetic characterizations were performed by PPMS (PPMS-9T, Quantum Design). The UV–vis diffuse reflectance spectra were obtained using a Varian Cary 500 scan UV–vis spectrophotometer equipped with an integrating sphere assembly. During the measurement, $BaSO_4$ was used as the reference material and the analysis range from 200 nm to 800 nm. Photo luminescence spectroscopy measurements were performed on Hitachi F-4500 with the excitation wavelength of 375 nm. The photocatalytic activity of the BSFO nanoparticles for decomposition of methyl orange (MO) was tested under irradiation of a Mercury Lamp (300 W) at the pH of 7. The initial concentration of MO was 20 mg/L with a catalyst loading of 30 mmol/L.

3. Results and discussion

3.1. Morphology

The morphology of the BSFO is shown in Fig. 1. Compared with the synthesis condition in Fig. 1(A) and (B), it demonstrates that ultrasonic irradiation can reduce the size (according to the histogram plot of the particle size distribution in Fig. 1(C), the average size decreases from 77.7 nm to 51.7 nm). The effect of ultrasonic irradiation can be explained by the procedure of reaction in Fig. 2. Since the ultrasonic wave can produce energy to form, expand, shrink and collapse bubbles, the release of magnitude energy from bubbles collapse increases the rate of the crystal nucleus. When the temperature is up to 250 °C, the reaction begins and the monomers are forming. With large energy releasing, the formed monomers are growing quickly to form nanoparticles till the reaction finishes. In comparison with the particles synthesized without ultrasonification, the amount of the crystal nucleus increased dramatically with ultrasonification, hence the formed nanoparticles are more homogeneous and smaller [23].

The uniform morphology of $Bi_{0.8}Sr_{0.2}FeO_{3-\delta}$ nanoparticles is shown in Fig. 1(D). The inset of shows the TEM image of a single $Bi_{0.8}Sr_{0.2}FeO_{3-\delta}$ nanoparticle, which has a size of 25 nm. This number agrees well the mean crystallite sizes of BSFO in Table 1.

3.2. Structure

All XRD results reveal the formation of single phase material in BSFO in Fig. 3. In Table 1, a systematic change in crystal structure from rhombohedral to pseudo-tetragonal with the rise of Sr^{2+} substitution is observed. It demonstrates that the crystal size gradually decreases with the increase of Sr^{2+} dopant concentration, which could be attributed to the doping ions into the BFO lattice that inhibits the grain growth [24].

As a metastable structure, the impurities always appear in the Bi_2O_3-Fe_2O_3 system. According to the XRD patterns of BSFO (Fig. 3), some impurities exist in nanoparticle. However, it is obvious that impurities decrease with the increase of Sr^{2+} dopant concentration. This might be due to the Sr^{2+} cation compensating the evaporation of Bi^{3+} cation.

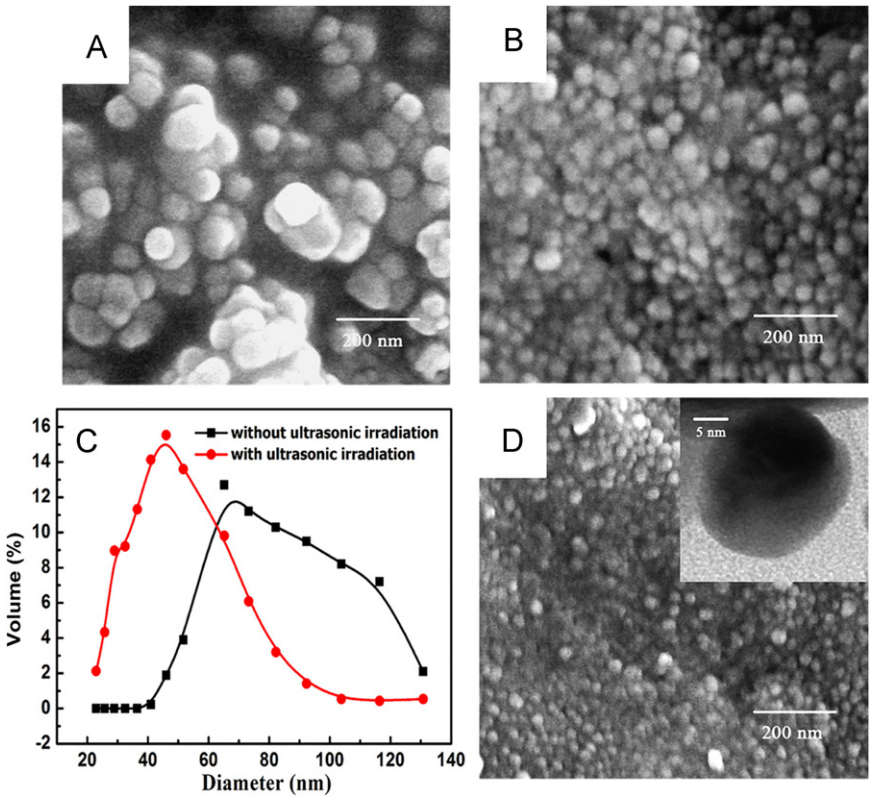

Fig. 1. The morphology of BFO synthetized without (A) and with (B) ultrasonification; (C) The particle size distribution analyzed from (A) and (B); (D) The morphology of $Bi_{0.8}Sr_{0.2}FeO_{3-\delta}$.

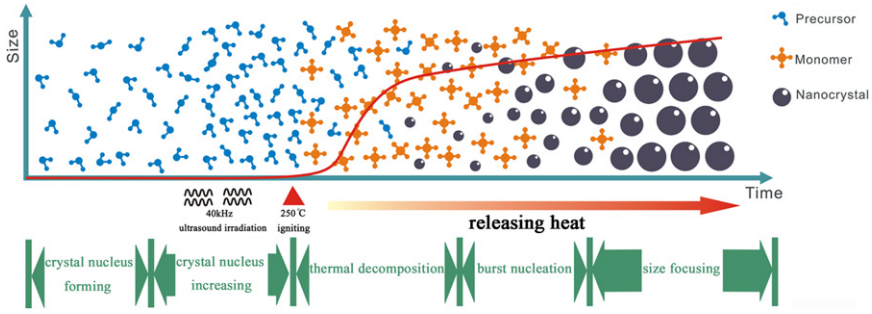

Fig. 2. Schematic illustration of the procedure of reaction.

Table 1
The suggested crystal symmetry and unit cell parameters of BSFO systems.

Sample	Crystal symmetry	S.G	Unit cell parameter (Å)			Crystal size
			a_{hex}	b_{hex}	c_{hex}	(Å)
$X=0$	Rhombohedral	R3c	5.569	5.586	13.84	378
$X=0.05$	Triclinic	P1	5.607	5.642	6.916	327
$X=0.1$	Pseudo-tetragonal	P4/mmm	3.956	3.956	3.956	229
$X=0.2$	Pseudo-tetragonal	P4/mmm	3.954	3.954	3.954	220

Yuan et al. reported that rhombohedral structure with space group R3c could be treated as a special triclinic structure [25]. Table 1 illustrates the structure transformation from rhombohedral to pseudo-tetragonal. As shown in XRD patterns of Fig. 4(A), the split peaks in 2θ ranges of 31°–33° merge gradually to form a broad peak (110) with the content

of Sr^{2+} increase. When $x \geq 0.1$, all splitting peaks disappear indicating the single-phase structure of pseudo-tetragonal is formed.

It is noticeable that the unit cell parameters of BSFO ($x \geq 0.1$) can be indexed on the basis of a cubic perovskite unit cell of $SrFeO_{2.97}$ [26]. The cell parameters of BSFO between $0 \leq x \leq 0.1$ is also shown in Fig. 4(B). It is shown that c/a decreases with the increase of Sr^{2+} dopant concentration. For $x=0.1$, c/a=1 indicates a single structure of pseudo-tetragonal is formed. This phenomenon described above is quite similar to the description of Wang et. al [18] and Golubeva et. al [26], but it is interesting to notice that the doping content point of structure transformation is different. Wang et al. reported that a whole pseudo-tetragonal structure when $x=0.2$ [18], which is different from that discussed above. This could be attributed to the nano-effect [21]. When the particle size decreases, the lattice parameters deviate from bulk, implying the structure is approaching a cubic perovskite structure. Hence, the nano-effect is responsible for the c/a decrease that brings forward the structure transformation by doping.

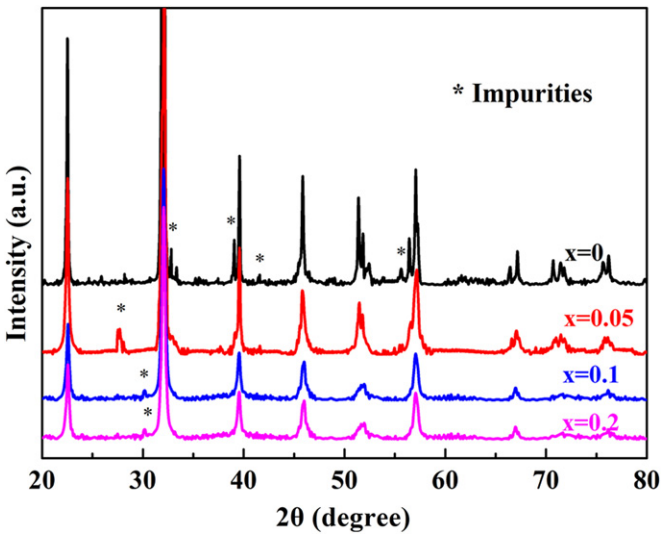

Fig. 3. The XRD patterns of BSFO at room temperature.

3.3. Magnetization

The influence of Sr^{2+} ions doping on BFO nanoparticles *magnetization* is further studied here. As shown in Fig. 5, a typical ferromagnetic character appears on the magnetic hysteresis loops of BSFO with an applied field of 10 kOe. It is implied that Sr^{2+} ions doping enhances the magnetization of BFO. The value of saturated magnetization (*Ms*) has been greatly improved compared with the bulk BFO (0.03 emu/g) [27] and $Bi_{0.8}Sr_{0.2}FeO_{3-\delta}$ (0.14 emu/g) [28].

The main reason for the enhancement of magnetization can be explained by the nano-effect and doping 0theory. As Bi sites were substituted for heterovalent Sr^{2+} ions, the imbalance of charge would result in the existence of oxygen vacancies. These oxygen vacancies suppress the spiral spin structure of BFO, leading to the appearance of weak ferromagnetism. Moreover, the model of magnetization of the BFO nanoparticles could be described as the presence of the exchange coupling between the ferromagnetic surfaces and the antiferromagnetic cores [21]. The

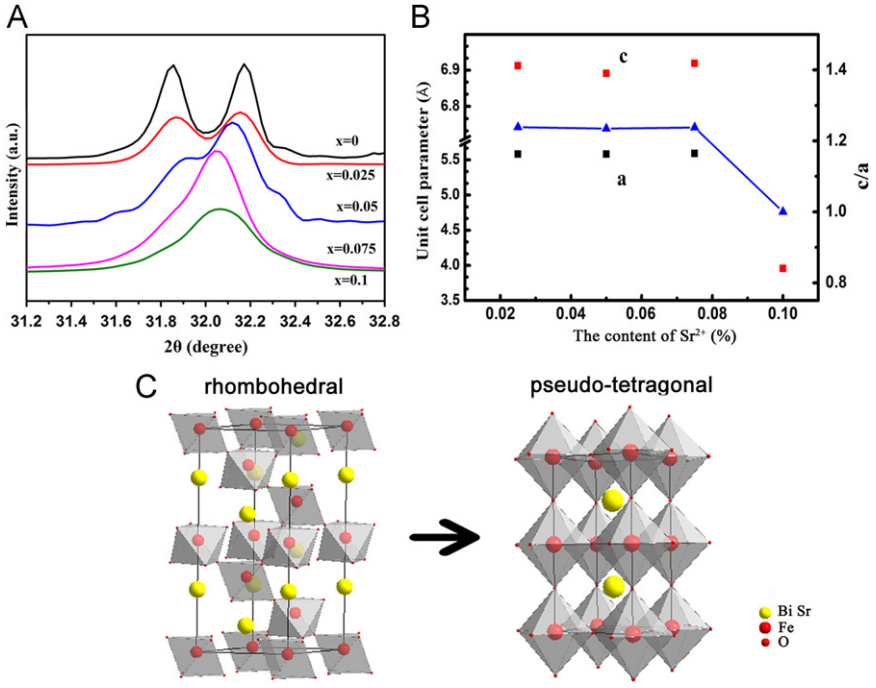

Fig. 4. (A) The XRD patterns of BSFO between $0 \leq x \leq 0.1$ in the range of 31°–33°; (B) The comparison of cell parameters of BSFO between $0 \leq x \leq 0.1$;(C) Schematic representation of the transformation of BSFO.

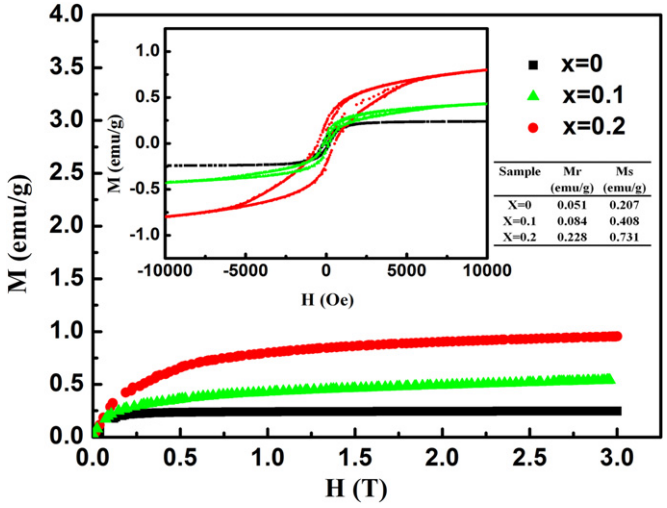

Fig. 5. *M–H* curves of BSFO nanoparticles at room temperature.

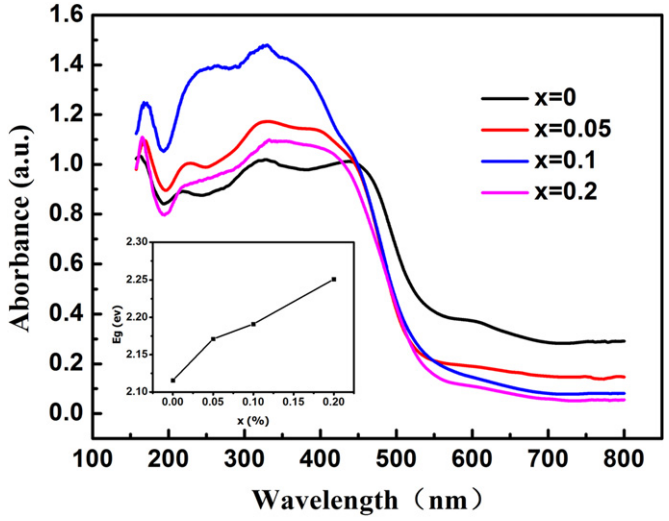

Fig. 6. UV–vis absorbance spectrum of BSFO nanoparticles. The inset shows the curve of the bandgap vs. Sr^{2+} concentration.

Table 2
Magnetic parameters derived from *M* vs *H* curves at room temperature.

Sample	*d* (nm)	M_{FMs} (emu/g)	χ_{AF} (emu/g Oe)
$X=0$	37.8	0.229	1.44×10^{-7}
$X=0.1$	22.9	0.347	7.61×10^{-6}
$X=0.2$	22	0.732	1.21×10^{-5}

long-range antiferromagnetic order is interrupted by the surface. When the size of particles decreases, the larger surface makes the spins more uncompensated that enhances the particles' overall magnetization.

In order to illustrate further, Fig. 5 shows the curves of *M* versus *H* at room temperature. A formula is used for represent data [29]:

$$M(H) = M_{FM}(H) + \chi_{AF}(H) \quad (1)$$

The saturation value M_{FMs} of $M_{FM}(H)$ is described by the intercept of the linear fit to the high field susceptibility with the zero field axis, it stands for two contributions of the spontaneous magnetization of ferromagnet. One is that the Sr^{2+} ions substitution cant the spins, the other is from the ferromagnetic shell influenced by the surface range. χ_{AF}, reflecting antiferromagnet over random grain distribution, is the high field slope ($H > 0.5$ T) describing the linear portion of the curve. The calculated values of M_{FMs} and χ_{AF} increasing with the decrease of the size of the particle are shown in Table 2, which accord well with the description of Jia et. al [23]. This result proves that M_{FMs} and χ_{AF} are related with the size, and the magnetization can be enhanced by decreasing the size of particles and increasing the content of Strontium substitution.

3.4. Photocatalyst

MO, as a typical organic contaminant, is often eliminated under UV–vis irradiation by the photocatalysts. BFO is a novel photocatalyst under visible-light illumination [6,30].

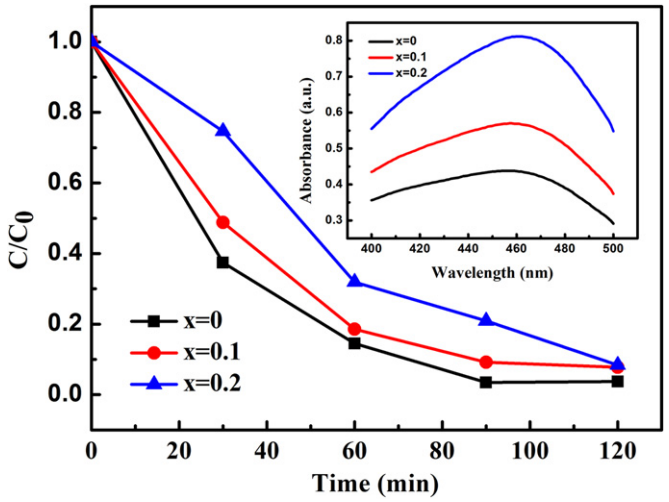

Fig. 7. Photocatalytic ability of different BSFO nanoparticles, the inset shows the UV–vis absorbance spectrum of MO with BSFO nanoparticles for different photocatalytic reaction times.

The UV–vis absorption spectra of BSFO are shown in Fig. 6. As the Sr^{2+} dopant increase, the absorption cut off wavelength of as-prepared BSFO shows a blue shift from 575 nm to 545 nm suggesting that all the series samples can absorb visible light in the wavelength range of 400–580 nm. The optical energy bandgap for different samples is determined by the Kubelka–Munk (K–M) theory. For a comparison of different samples, the optical energy bandgap increases from 2.15 eV–2.26 eV with the increase of Sr^{2+} dopant concentration. This is because foreign elements change the band structure of BFO so that it makes the rearrangement of the molecular orbitals.

The concentration of MO under UV–vis light irradiation is also tested with existence of nanoparticles. In Fig. 7, MO can be degraded by each sample under UV–vis light irradiation. It is well fitted with the bandgap. As the bandgap increases, the ability of photocatalyst declines.

However, all doping samples still show the encouraging photocatalytic ability. After 2 h irradiation, the degradation rate (C/C_0) of all samples decreases below 0.2. With ultrasonic irradiation, lots of defections arise on the surface of the nanoparticles. These defections are beneficial to the adsorption of oxygen and promoting the photocatalytic reaction [30].

4. Conclusion

A novel ultrasonic irradiation assisted self-combustion method was used to synthesize Sr^{2+}-doped BFO nanoparticles. The average size of the nanoparticles decreased with the increase of Sr^{2+} dopant concentration. It was found that the lattice structure transformed from the rhombohedral structure ($x=0$) to the pseudo-tetragonal structure ($x \geq 0.1$). Owing to the smaller particles, the nano-effect helped c/a decrease that brought forward the structure transformation with doping. The improved ferromagnetic ordering of BFO nanoparticles with doping might be due to the nano-effect and Sr^{2+} substitution. The result of photocatalytic tests showed that all samples exhibited promising photocatalytic ability with more defections and surface.

Acknowledgments

The authors would like to acknowledge the support of the project funded by the Priority Academic Program Development (PAPD) of Jiangsu Higher Education Institutions and the National Natural Science Foundation of China (No. 20771079).

References

[1] S-W. Cheong, M. Mostovoy, Multiferroics: a magnetic twist for ferroelectricity, Nature Materials 6 (2007) 13–20.
[2] W. Eerenstein, N. Mathur, J. Scott., Multiferroic and magnetoelectric materials, Nature 442 (2006) 759–765.
[3] F. Gao, X. Chen, K. Yin, S. Dong, Z.F. Ren, F. Yuan, T. Yu, Z.G. Zou, J.M. Liu, VisibleLight Photocatalytic Properties of Weak Magnetic $BifeO_3$ Nanoparticles, Advanced Materials (Weinheim, Germany) 19 (2007) 2889–2892.
[4] W. Ji, K. Yao, Y.C. Liang, Bulk photovoltaic effect at visible wavelength in epitaxial ferroelectric $BiFeO_3$ thin films, Advanced Materials (Weinheim, Germany) 22 (2010) 1763–1766.
[5] A.R. Damodaran, C.W. Liang, Q. He, C.Y. Peng, L. Chang, Y.H. Chu, L.W. Martin, Nanoscale Structure and Mechanism for Enhanced Electromechanical Response of Highly Strained $BiFeO_3$ Thin Films, Advanced Materials (Weinheim, Germany) 23 (2011) 3170–3175.
[6] J. Li, Y. Duan, H. He, D. Song, Crystal structure, electronic structure, and magnetic properties of bismuth-strontium ferrites, Journal of Alloys and Compounds 315 (2001) 259–264.
[7] V.A. Khomchenko, M. Kopcewicz, A.M.L. Lopes, Y.G. Pogorelov, J.P. Araujo, J.M. Vieira, A.L. Kholkin, Intrinsic nature of the magnetization enhancement in heterovalently doped Bi1−xAxFeO3 (A=Ca, Sr, Pb, Ba) multiferroics, Journal of Physics D: Applied Physics 41 (2008) 102003.
[8] B. Kundys, A. Maignan, C. Martin, N. Nguyen, C. Simon, Magnetic field induced ferroelectric loop in $Bi_{0.75}Sr_{0.25}FeO_{3-\delta}$, Applied Physics Letters 92 (2008) 112905.
[9] E. Folcke, J.M. Le Breton, JM Bréard, Y Maignan, A. Mössbauer spectroscopic analysis of $Bi_{1-x}Sr_xFeO_{3-\delta}$ perovskites, Solid State Sciences 12 (2010) 1387–1392.
[10] I Troyanchuk, M. Bushinsky, D. Karpinsky, V. Sirenko, V. Sikolenko, V. Efimov, Structural and magnetic phases of $Bi_{1-x}A_xFeO_{3-\delta}$ (A=Sr, Pb) perovskites, European Physical Journal B 73 (2010) 375–381.
[11] C Ederer, N.A Spaldin, Influence of strain and oxygen vacancies on the magnetoelectric properties of multiferroic bismuth ferrite, Physical Review B 71 (2005) 224103.
[12] J.M. Wesselinowal, I. Apostolova, Theoretical study of multiferroic $BiFeO_3$ nanoparticles, Journal of Applied Physics 104 (2008) 084108.
[13] T.J. Park, G.C. Papaefthymiou, A.J Viescas, A.R. Moodenbaugh, S.S Wong, Size-dependent magnetic properties of single-crystalline multiferroic $BiFeO_3$ nanoparticles, Nano Letters 7 (2007) 766–772.
[14] A. Jaiswal, R. Das, K. Vivekanand, P.M. Abraham, S. Adyanthaya, P. Poddar, Effect of Reduced Particle Size on the Magnetic Properties of Chemically Synthesized $BiFeO_3$ Nanocrystals, Journal of Physical Chemistry C. 114 (2010) 2108–2115.
[15] S.M. Selbach, T. Tybell, M.A. Einarsrud, T. Grande, Size-dependent properties of multiferroic $BiFeO_3$ nanoparticles, Chemistry of Materials : A Publication of the American Chemical Society 19 (2007) 6478–6484.
[16] D.P. Dutta, O.D. Jayakumar, A.K. Tyagi, K.G. Girija, C.G.S. Pillai, G. Sharma, Effect of doping on the morphology and multiferroic properties of $BiFeO_3$ nanorods, Nanoscale 2 (2010) 149–1154.
[17] Z.K. Liu, Y.J. Qi, C.J. Lu, High efficient ultraviolet photocatalytic activity of $BiFeO_3$ nanoparticles synthesized by a chemical coprecipitation process, Journal of Materials Science—Materials in Electronics 21 (2010) 380–384.
[18] Y.G. Wang, G. Xu, Z.H. Ren, X. Wei, W.J. Weng, P.Y. Du, G. Shen, G.R. Han, MineralizerAssisted Hydrothermal Synthesis and Characterization of $BiFeO_3$ Nanoparticles, Journal of the American Ceramic Society 90 (2007) 2615–2617.
[19] F. Deganello, G. Marcì, G. Deganello, Citrate–nitrate auto-combustion synthesis of perovskite-type nanopowders: A systematic approach, Journal of The European Ceramic Society 29 (2009) 439–450.
[20] J.C. Yu, J. Yu, W. Ho, L. Zhang, Preparation of highly photocatalytic active nano-sized TiO_2 particles via ultrasonic irradiation, Chemical Communications 19 (2001) 1942–1943.
[21] F.Z. Qian, J.S. Jiang, S.Z. Guo, D.M. Jiang, W.G. Zhang, Multiferroic properties of $Bi_{1-x}Dy_xFeO_3$ nanoparticles, Journal of applied physics 106 (2009) 106 084312.
[22] K. Chakrabarti, K. Das, B. Sarkar, S.K. De, Magnetic and dielectric properties of Eu-doped $BiFeO_3$ nanoparticles by acetic acid-assisted sol-gel method, Journal of Applied Physics 110 (2011) 103905.
[23] L.S. Jia, T. Ding, Q.B. Li, Y. Tang, Study of photocatalytic performance of $SrFeO_{3-x}$ by ultrasonic radiation, Catalysis Communications 8 (2007) 963–966.
[24] A. Watcharapasorn, S. Jiansirisomboon, Grain growth kinetics in Dy-doped $Bi_{0.5}Na_{0.5}TiO_3$ ceramics, Ceramics International 34 (2008) 769–772.
[25] G.L. Yuan, S.W. Or, Multiferroicity in polarized single-phase $BiSmFeO_3$ ceramics, Journal of Applied Physics 100 (2006) 024109.
[26] O.Y. Golubeva, V.G. Semenov, V.S. Volodin, V.V. Gusarov, Structural stabilization of Fe^{4+} Ions in perovskite-like phases based on the $BiFeO_3$–$SrFeO_y$ system, Glass Physics and Chemistry 35 (2009) 313–319.
[27] A.K. Pradhan, K. Zhang, D. Hunter, J.B. Dadson, G.B. Loiutts, P. Bhattacharya, R. Katiyar, J. Zhang, D.J. Sellmyer, U.N. Roy, Magnetic and electrical properties of single-phase multiferroic $BiFeO_3$, Journal of Applied Physics 97 (2005) 093903.

[28] L.W. Wang, D.H. Wang, H.B. Huang, Q.Q. Han, B.X. Cao, Y.W. Du, The magnetic properties of polycrystalline $Bi_{1-x}Sr_xFeO_3$ ceramics, Journal of Alloys and Compounds 469 (2009) 1–3.

[29] C. Ma, J.Q. Yan, K. Dennis, K, R. McCallum, X. Tan, Size-dependent magnetic properties of high oxygen content $YMn_2O_{5\pm\delta}$ multiferroic nanoparticles, Journal of Applied Physics 105 (2009) 033908.

[30] C.M. Cho, J.H. Noh, I.S. Cho, J.S. An, K.S. Hong, J.Y. Kim, Low-Temperature Hydrothermal Synthesis of Pure $BiFeO_3$ Nanopowders Using Triethanolamine and Their Applications as Visible-Light Photocatalysts, Journal of the American Ceramic Society 91 (2008) 3753–3755.